

Double-differential cross sections for the neutron production from heavy-ion reactions at energies $E/A = 290\text{--}600$ MeV

Y. Iwata* and T. Murakami

Department of Accelerator Physics and Engineering, National Institute of Radiological Sciences, 4-9-1 Anagawa, Inage, Chiba 263-8555, Japan

H. Sato, H. Iwase, T. Nakamura, and T. Kurosawa[†]

Cyclotron and Radioisotope Center, Tohoku University, Aoba, Aramaki, Sendai 980-8578, Japan

L. Heilbronn

Lawrence Berkeley National Laboratory, Berkeley, California 94720

R. M. Ronningen

National Superconducting Cyclotron Laboratory, Michigan State University, East Lansing, Michigan 48824-1321

K. Ieki and Y. Tozawa

Department of Physics, Rikkyo University, 3 Nishi-Ikebukuro, Toshima, Tokyo 171-8501, Japan

K. Niita

Research Organization for Information Science and Technology, Tokai, Nara, Ibaraki 319-1195, Japan

(Received 28 June 2001; published 12 October 2001)

We have measured the double-differential cross sections for neutron production from C, Ne, and Ar projectiles at $E/A = 290\text{--}600$ MeV on C, Cu, and Pb targets. Neutron energies were measured at laboratory angles between 5° and 80° . The measured neutron spectra have three components. At forward angles, a prominent peak originating from the projectile-fragmentation process was observed. The velocity of neutrons corresponding to the peak was about the same as that of the projectile. In addition to the peak, two components of Maxwellian-shape distributions corresponding to the preequilibrium and equilibrium processes were observed. By fitting with a moving-source model having three components, the neutron spectra were fairly well described. The parameters obtained for each component are consistent with a picture of the projectile fragmentation, preequilibrium, and equilibrium processes. By integrating the fitted functions with respect to the neutron energies and solid angles, the angular distributions and total cross sections for the neutron production were determined. The neutron spectra, angular distributions, and total cross sections were compared with those calculated by the quantum molecular dynamics and heavy-ion codes. We found that neither of the codes could reproduce the measured cross sections for all combinations of the projectiles and targets.

DOI: 10.1103/PhysRevC.64.054609

PACS number(s): 25.70.Mn, 24.10.-i, 28.20.-v, 87.52.Ga

I. INTRODUCTION

Due to the recent developments in accelerator technology, relativistic heavy-ion beams have become available. Applications of these accelerators include medical treatment, as well as nuclear structure and reaction studies. Not only are primary beams directly used, but also radioactive nuclear beams, produced by fragmentation processes, are utilized. The advent of radioactive nuclear beams has realized the use of unstable nuclei.

With increasing energy and intensity of the beams, the importance of radiation shielding has greatly increased in designing new facilities. Among the radiation hazards, neu-

trons from heavy-ion reactions at high energies play a key role in the shielding design because of their large attenuation lengths in shielding materials. In designing radiation shielding, transport codes are used to estimate the production and transport of neutrons through shielding materials. Cross sections of neutron production used in these codes were compared with experimental data, such as Refs. [1–7]. Unfortunately, these data were obtained by measurements where heavy ions stopped in thick targets [1–7]. It is obvious, however, that the differential cross sections obtained using thin targets are more suited for the purpose of direct comparison with models, because the codes calculate the cross sections for each step of the collision. Although several measurements of cross sections have been reported [8–11], cross section data are scarce and no systematic data exist. Therefore, cross section measurements are necessary for rigorous tests of these codes.

In this paper, we report systematic measurements of neutron-production cross sections from C, Ne, and Ar projectiles having $E/A = 290\text{--}600$ MeV on C, Cu, and Pb tar-

*Present address: Japan Science and Technology Corporation (JST). Corresponding address: NIRS, 4-9-1 Anagawa, Inage, Chiba 263-8555, Japan. Electronic address: y_iwata@nirs.go.jp

[†]Present address: Electrotechnical Laboratory, 1-1-4, Umezono, Tsukuba, Ibaraki, 305-8568 Japan.

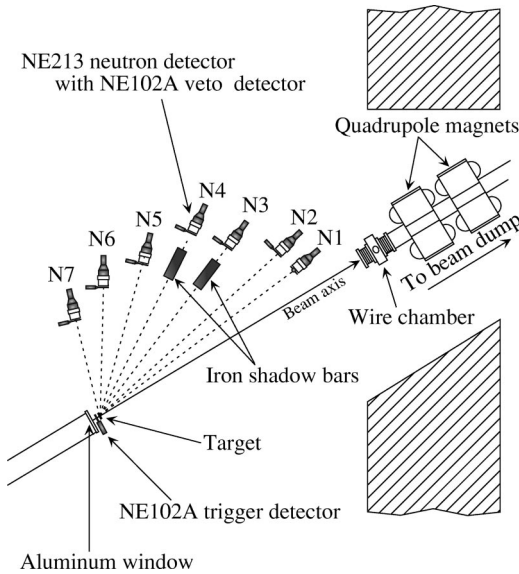


FIG. 1. Schematic drawing of the experimental setup.

gets. Neutron-energy spectra were measured between 5° and 80° . The spectra could be reproduced by a moving-source model assuming three components; the model has been fairly successful in describing inclusive energy spectra of fragments [12–15]. The three components may be attributed to projectile fragmentation, preequilibrium, and equilibrium processes. By integrating fitted curves with respect to the neutron energy and solid angles, the angular distributions and total cross sections for the neutron production were evaluated. Furthermore, the measured spectra were compared with those calculated by the quantum molecular dynamics (QMD) [16] or heavy-ion code (HIC) [17]. We found, as reported in Refs. [9–11], that neither of the model calculations provided good agreement with the measured cross sections for whole combinations of the projectiles and targets.

II. EXPERIMENTAL PROCEDURES

The experiment was carried out at the Heavy Ion Medical Accelerator in Chiba (HIMAC) facility of the National Institute of Radiological Sciences (NIRS), Japan [18,19]. A schematic drawing of the experimental setup is shown in Fig. 1. Heavy ions of C, Ne, and Ar were accelerated to $E/A = 290$ – 600 MeV by HIMAC and transported to an experi-

ment room by the high-energy beam transport (HEBT) system. The HEBT system provided an approximately parallel beam with a spot size of a few millimeter in diameter on the target. A pulsed beam, whose time duration was 0.6 – 1.0 s, dependent on ion species and energies, was delivered every 3.3 s. In order to reduce the pileup events and to keep the dead time of the data-acquisition system at a tolerable level, the beam intensity was kept at a few times 10^4 – 10^5 particles per pulse. The live time was determined by the ratio of the number of events recorded in the data-acquisition system to the number of events counted by the scaler modules. The live time was about 80 – 90% during the experiment. Furthermore, events in which the trigger detector was fired more than once within the coincidence between the projectile and neutron were excluded in the offline analysis. These events were less than 10% of the total events, depending on the beam intensity.

As shown in Fig. 1, the beam emerged from a vacuum beam line of the HEBT system, passing through an $100\text{-}\mu\text{m}$ -thick aluminum window. Before impinging on the target, the beam traversed a trigger detector, 0.5 mm thick and 30 mm in diameter, made of an NE102A plastic scintillator. The number of incident particles, which were used to normalize the cross sections, was counted by the detector. Downstream from the target, the beam traversed air and stopped at a beam dump placed about 20 m downstream from the target in another shielded room. In order to minimize the background, the beam was focused on the center of the beam dump by the set of quadrupole magnets located between the two shielded rooms as shown in Fig. 1.

The neutrons were measured by a NE213 liquid scintillator, whose container had a cylindrical shape of 127 mm in diameter and 127 mm in thickness. Seven detectors, N1–N7, were arranged at laboratory angles between 5° and 80° with respect to the beam direction. A veto detector, 127 mm \times 127 mm \times 5 mm, made of NE102A plastic scintillator, was placed directly in front of each neutron detector. The neutron energies were determined by the time-of-flight (TOF) method. While a good energy resolution is essential for detectors placed at forward angles, sufficient statistics, i.e., employing large solid angles, are more important at backward angles. Therefore, the flight path L was chosen to be 506 cm at forward angles and was decreased as laboratory angles increased, as summarized in Table I. The flight path is

TABLE I. Summary of the neutron detectors.

Detectors	θ (deg)	L (cm)	Energy resolution $\Delta E/E$ (%) for neutrons at		
			200 MeV	400 MeV	600 MeV
N1	5	506	7.75	10.7	13.8
N2	10	506	7.75	10.7	13.8
N3	20	456	8.60	11.8	14.4
N4	30	456	8.60	11.8	14.4
N5	40	406	9.66	13.3	17.3
N6	60	356	11.0	15.2	19.7
N7	80	306	12.8	17.7	22.9

TABLE II. Summary of the beams and targets used in the experiment.

Beam (MeV)	Thickness (g/cm ²)		
	C target	Cu target	Pb target
C at $E/A=290$	1.80	4.47	2.27
C at $E/A=400$	9.00	13.4	9.08
Ne at $E/A=400$	1.80	4.47	2.27
Ne at $E/A=600$	3.60	4.47	4.54
Ar at $E/A=400$	0.720	1.34	1.70
Ar at $E/A=560$	1.08	1.79	2.27

the distance from the target to the center of the liquid scintillator cell.

The TOF for each neutron was measured using the time difference between signals from the trigger detector and neutron detector. The time difference was digitized by a time-to-digital converter and recorded event by event. The absolute time was determined by referring to the distribution of prompt γ rays produced by beam particles striking the target. The time resolution Δt was estimated from the width of the γ -ray peak and found to be approximately 1 ns in full width at half maximum. With Δt and the thickness of the neutron detector, $\Delta L=127$ mm, the energy resolution was estimated to be

$$\frac{\Delta E_n}{E_n} = \frac{E_n + M_n}{E_n} \frac{\beta^2}{1 - \beta^2} \sqrt{\left(\frac{\Delta L}{L}\right)^2 + \left(\frac{\Delta t}{t}\right)^2}, \quad (1)$$

where E_n and M_n are the kinetic energy and rest mass of a neutron, respectively. The energy resolutions, calculated using Eq. (1) for 200, 400, and 600 MeV neutrons, are shown in Table I.

The target thickness was chosen so that the energy loss of the beam in the target would be 5–10 %, as summarized in Table II. An exception was the set of targets used for the C beam at $E/A=400$ MeV; the targets were relatively thick, corresponding to energy losses of 11–22 %.

Background events originating from charged particles were excluded using the data from the veto detectors. Each NE213 liquid scintillator detector had the capability of neutron/ γ discrimination via difference in pulse shape. The total and slow components of the pulse from each photomultiplier of the neutron detector were measured by a charge-integrating analog-to-digital converter (QDC). Figure 2 shows a plot of the charge-integrated total pulse Q_{tot} vs the slow component Q_{slow} . We can clearly distinguish neutrons and γ rays above $Q_{\text{tot}}=1$ MeVee in electron-equivalent energy (MeVee). The pulse-height threshold of the electronics was set to small values, approximately 1 MeVee for N1 through N3 and 0.5 MeVee for the others. In an off-line analysis, we adopted a threshold of 4 MeVee for N1 through N3 and 1 MeVee for the others.

Two shadow bars made of iron, 15×15 cm² and 60 cm long, were placed in front of two of the neutron detectors in order to estimate background neutrons, such as room-

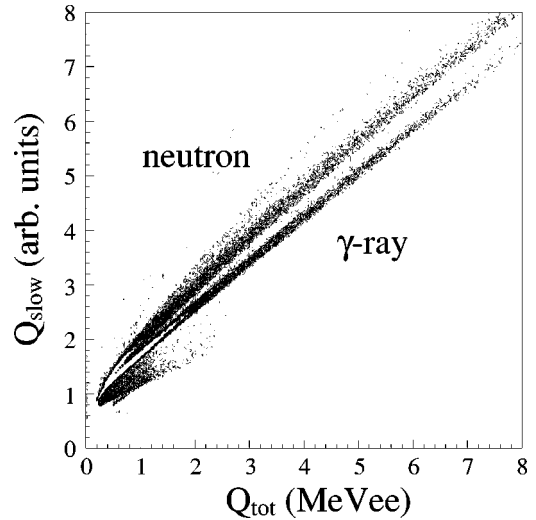


FIG. 2. Plot of the total pulse Q_{tot} versus the slow component Q_{slow} . The abscissa employs electron equivalent energy (MeVee). A clear difference is observed above $Q_{\text{tot}}=1$ MeVee.

scattered neutrons. Since the thickness of the shadow bars is sufficient to attenuate neutrons coming directly from the target, all of the neutrons measured with the shadow bars in place are considered as backgrounds. The contribution from background neutrons was subtracted in an off-line analysis. The shadow bars were moved periodically to the fronts of different detectors during the experiment, such that background data were obtained for all of the detectors.

The detection efficiency was calculated by a Monte Carlo simulation code [20]. Figure 3 shows the detection efficiencies calculated as functions of the neutron energies E_n . The solid and dashed curves correspond to the results with pulse-height thresholds E_{th} of 1 MeVee and 4 MeVee, respectively, which were the values used in the present analysis. While a difference between two curves is noticeable around $E_n=10$ MeV, it is rather small above $E_n=100$ MeV.

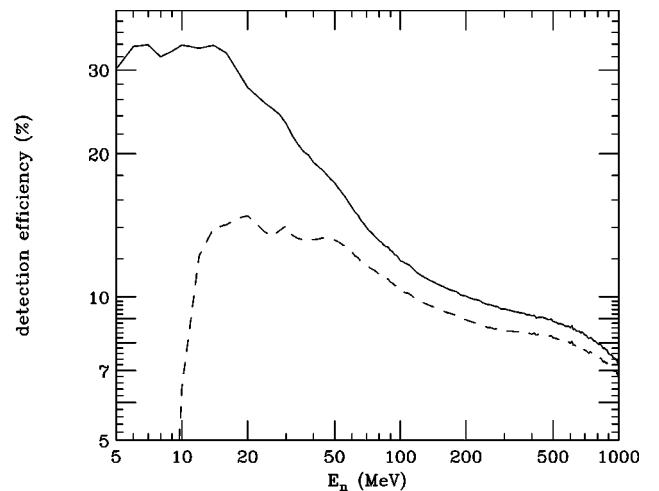


FIG. 3. Calculated detection efficiency as a function of the neutron energies E_n . The solid and dashed curves correspond to the results for pulse-height thresholds E_{th} of 1 MeVee and 4 MeVee, respectively.

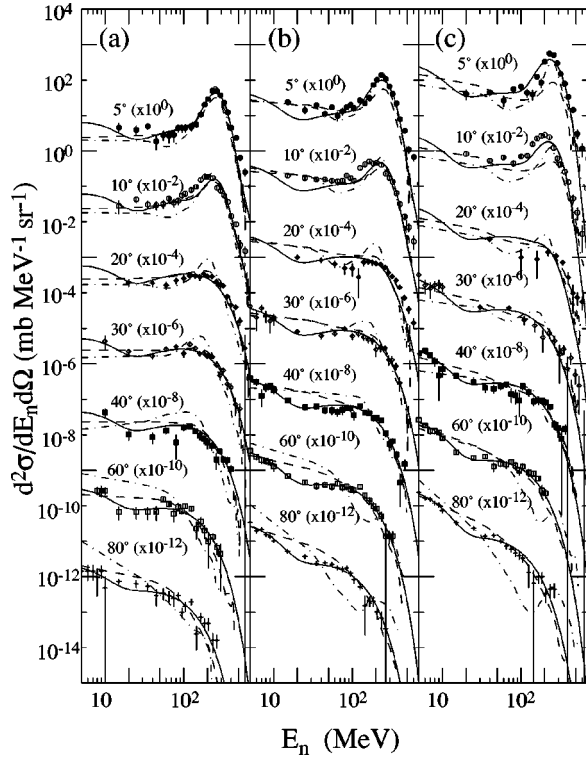


FIG. 4. Double-differential cross sections for the C beam at $E/A = 290$ MeV. The targets are (a) C, (b) Cu, and (c) Pb. The solid curves show the results calculated by the moving-source model. The dashed and dot-dashed curves show the results of the QMD and HIC calculations, respectively.

III. EXPERIMENTAL RESULTS

A. Double-differential cross sections

The double-differential cross sections are shown by symbols in Figs. 4–9 as functions of the neutron energies measured in the laboratory frame. The energy spectra measured at 5° show a prominent peak. This peak is less pronounced at 10° and is insignificant at 20° and larger. The velocity of the neutrons corresponding to the peak is approximately the same as that of the projectile. Thus, the origin of neutrons corresponding to the peak seems to be from the projectile-fragmentation process. In addition to the peak from projectilelike neutrons, it seems that two components exist for all of the spectra: one is a shoulder below $E_n = 20$ MeV; the other is a wide peak extending up to a few hundreds MeV. The energy spectra below $E_n = 20$ MeV show an almost identical shape and cross sections for all of the spectra. Since these neutrons have an isotropic distribution in the laboratory frame, they could be attributed to evaporation from target residues through the equilibrium process. The other component becomes less pronounced with increasing angles. This component may reflect the preequilibrium process. We noticed that the three components exist for all combinations of the targets and projectiles.

The error bars in Figs. 4–9 include statistical uncertainty only. The major sources of the systematic uncertainty are classified as follows: (1) uncertainty of the target thickness; (2) attenuation of neutrons in the target and in the air; (3) uncertainty of the calculated detection efficiency; and (4)

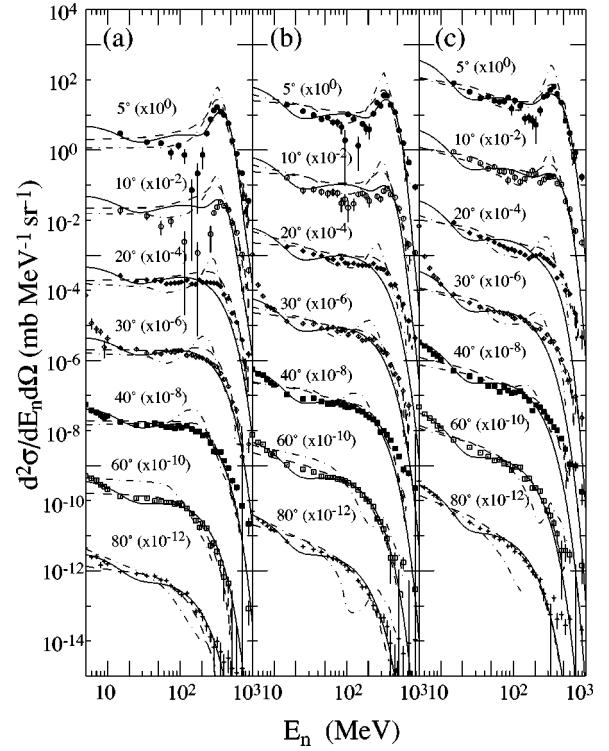


FIG. 5. Double-differential cross sections for the C beam at $E/A = 400$ MeV. See caption of Fig. 4.

neutrons produced in the aluminum window, the trigger detector, and the air.

The densities of the targets were determined from the size and mass. Measurements of several samples revealed that the

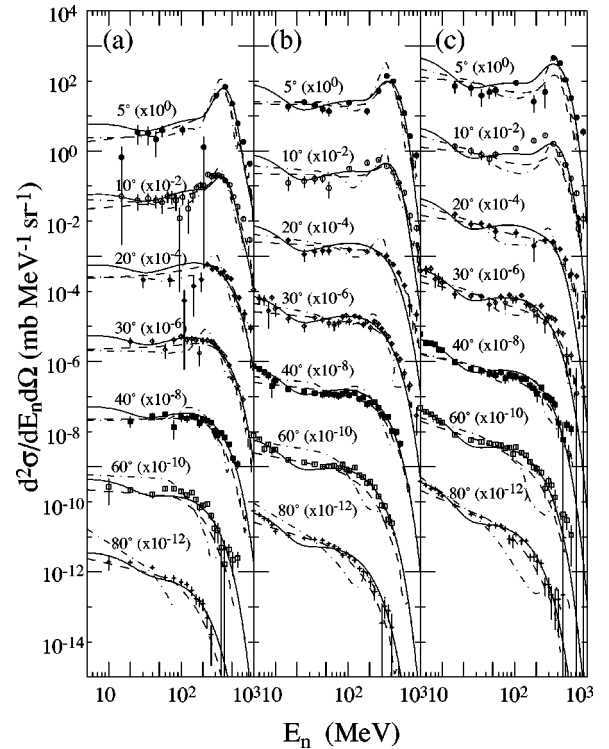


FIG. 6. Double-differential cross sections for the Ne beam at $E/A = 400$ MeV. See caption of Fig. 4.

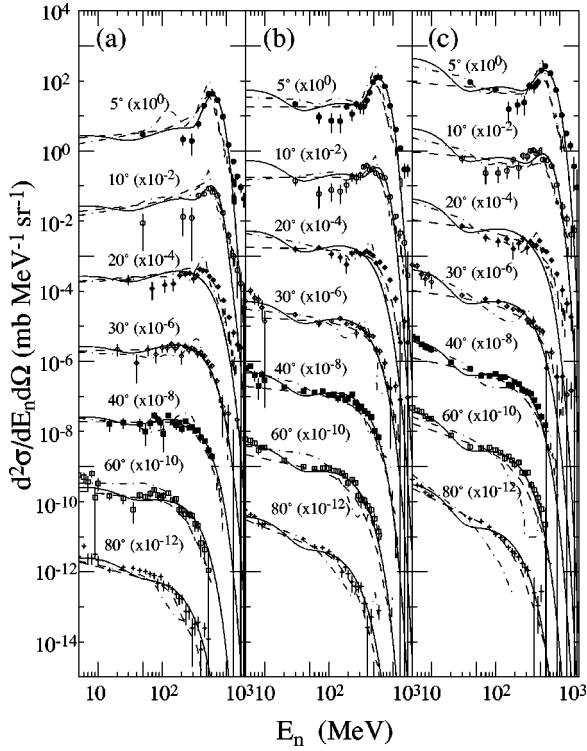


FIG. 7. Double-differential cross sections for the C beam at $E/A = 600$ MeV. See caption of Fig. 4.

uncertainty in the target thickness was about 6.8%, 2.5%, and 4.6% for the C, Cu, and Pb targets, respectively. The attenuation lengths, which are constant for neutrons with $E_n \geq 100$ MeV, are about 37, 16, and 18 cm for C, Cu, and

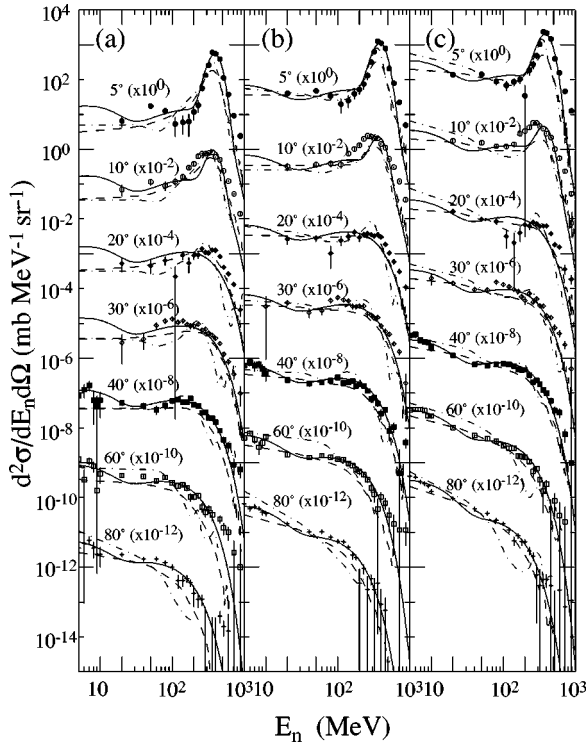


FIG. 8. Double-differential cross sections for the Ar beam at $E/A = 400$ MeV. See caption of Fig. 4.

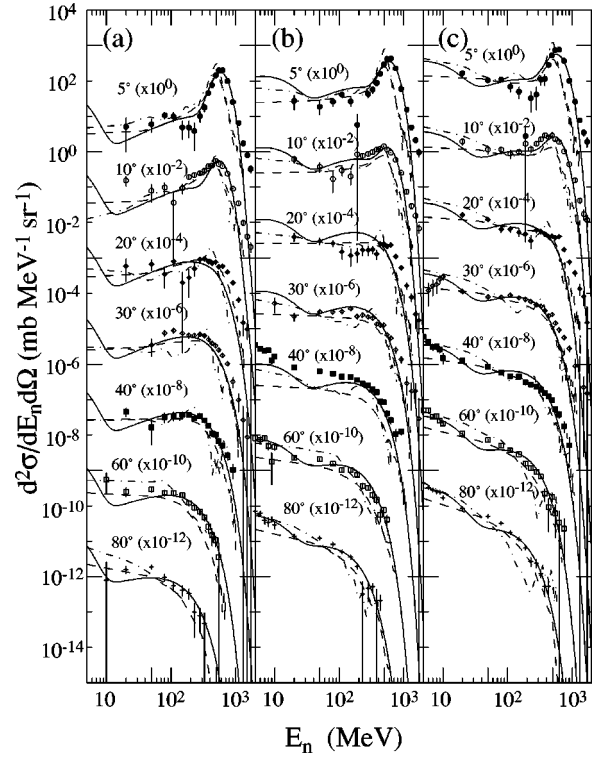


FIG. 9. Double-differential cross sections for the Ar beam at $E/A = 560$ MeV. See caption of Fig. 4.

Pb, respectively. The attenuation of neutrons was calculated by using these values. The attenuation is negligible in the air compared to the target. Whereas the uncertainty of the detection efficiency is estimated to be about 4% in Ref. [20], a recent report showed that the uncertainty is about 10% [21]. We employed a value of 10% as the uncertainty of the detection efficiency in the present analysis. Contribution from neutrons produced in the 100- μ m-thick aluminum window, the 0.5-mm-thick trigger detector, and 6 m of air is not negligible. To estimate the contribution of these materials, a measurement without a target was carried out for an Ar beam at $E/A = 560$ MeV. We estimated the contributions for measurements other than the Ar beam by assuming that the yield of the neutrons from materials other than the target is determined by the ratio of the thickness of the target and other materials.

IV. DISCUSSION

A. Moving-source model

A moving-source model has been successful in describing inclusive spectra of fragments from heavy-ion reactions [12–15]. The model assumes that a set of nucleons, named a source, is moving with some velocity in the laboratory frame, and is emitting nucleons or fragments having a distribution that can be characterized by a temperature. The measured fragment spectra in the center-of-mass frame (c.m.) of the source was taken to be a Maxwellian distribution. By fitting to the spectra, the temperature and velocity of the source can be inferred.

TABLE III. Parameters obtained by the fit with the moving-source model.

Beam (MeV)	Target	Projectile fragmentation		Preequilibrium		Equilibrium	
		σ (MeV/c)	β	τ (MeV)	β	τ (MeV)	β
C at $E/A=290$	C	75.3 ± 1.1	0.615 ± 0.012	46.5 ± 1.1	0.362 ± 0.056	3.61 ± 0.49	0.0597 ± 0.0107
	Cu	81.4 ± 1.4	0.596 ± 0.013	47.3 ± 0.8	0.292 ± 0.054	3.74 ± 0.19	0.156 ± 0.044
	Pb	81.3 ± 1.7	0.594 ± 0.016	42.4 ± 1.1	0.225 ± 0.082	3.54 ± 0.17	0.00251 ± 0.00431
C at $E/A=400$	C	84.1 ± 0.8	0.690 ± 0.007	57.0 ± 0.6	0.333 ± 0.004	5.02 ± 0.33	0.0314 ± 0.0040
	Cu	86.1 ± 1.1	0.684 ± 0.001	53.8 ± 0.5	0.268 ± 0.003	3.64 ± 0.08	0.0210 ± 0.0015
	Pb	112 ± 3	0.668 ± 0.002	48.0 ± 0.5	0.196 ± 0.003	3.60 ± 0.04	0.0105 ± 0.0009
Ne at $E/A=400$	C	85.0 ± 1.4	0.701 ± 0.001	63.0 ± 1.1	0.427 ± 0.005	7.56 ± 0.67	0.0426 ± 0.0139
	Cu	98.9 ± 2.2	0.689 ± 0.002	62.1 ± 0.9	0.328 ± 0.005	3.86 ± 0.22	0.0222 ± 0.0039
	Pb	111 ± 3	0.676 ± 0.003	55.3 ± 1.3	0.269 ± 0.008	4.12 ± 0.16	0.0106 ± 0.0034
Ne at $E/A=600$	C	109 ± 1	0.796 ± 0.001	87.9 ± 2.1	0.436 ± 0.010	9.98 ± 0.82	0.00100 ± 0.01572
	Cu	114 ± 2	0.790 ± 0.001	82.1 ± 1.7	0.378 ± 0.007	6.98 ± 0.43	0.0313 ± 0.0068
	Pb	131 ± 3	0.781 ± 0.002	74.4 ± 1.7	0.303 ± 0.008	5.57 ± 0.18	0.0237 ± 0.0036
Ar at $E/A=400$	C	73.7 ± 0.4	0.706 ± 0.000	67.3 ± 1.9	0.416 ± 0.008	4.49 ± 0.25	0.0696 ± 0.0041
	Cu	76.2 ± 0.5	0.702 ± 0.001	69.0 ± 1.4	0.378 ± 0.006	6.29 ± 0.43	0.0140 ± 0.0091
	Pb	78.9 ± 0.7	0.701 ± 0.001	64.8 ± 1.2	0.341 ± 0.006	7.01 ± 0.25	0.00939 ± 0.00451
Ar at $E/A=560$	C	117 ± 1	0.784 ± 0.001	86.3 ± 3.2	0.463 ± 0.0125	1.49 ± 0.17	0.0198 ± 0.0045
	Cu	123 ± 1	0.785 ± 0.001	79.5 ± 1.6	0.432 ± 0.008	5.56 ± 0.21	0.0633 ± 0.0043
	Pb	136 ± 2	0.775 ± 0.001	80.3 ± 1.6	0.359 ± 0.008	6.87 ± 0.25	0.00915 ± 0.00449

Since the measured spectra exhibit three components, as mentioned previously, we assumed three kinds of sources. These are the projectile fragmentation, preequilibrium, and equilibrium processes. By assuming the Serber model [22] or sudden approximation, the prominent peak at forward angles is related to the internal motion of the nuclei and the process of projectile fragmentation. Therefore, we employed a Gaussian function to express the momentum distribution of neutrons from this process

$$\frac{d^2\sigma}{p_c^2 dp_c d\Omega_c} = N e^{-p_c^2/2\sigma^2}, \quad (2)$$

where p_c is the momentum of a neutron measured in the c.m. of the source and σ is a width parameter. On the other hand, the momentum distribution of the equilibrium and preequilibrium processes were assumed to have Maxwellian shape

$$\frac{d^2\sigma}{p_c^2 dp_c d\Omega_c} = N (2\pi m\tau)^{-3/2} e^{-p_c^2/2m\tau}, \quad (3)$$

where τ is the source temperature and m is the mass of a free nucleon. Using the above quantities, one obtains the energy distribution in the laboratory frame as

$$\frac{d^2\sigma}{dE_n d\Omega} = p E_c \frac{d^2\sigma}{p_c^2 dp_c d\Omega_c}, \quad (4)$$

where p is the neutron momentum measured in the laboratory frame and E_c is the total energy in the c.m. expressed as

$$E_c = \gamma(E - \beta p \cos \theta). \quad (5)$$

Here, θ is the laboratory angle, β is the velocity of the source, and $\gamma = 1/\sqrt{1-\beta^2}$.

The measured neutron spectra were fitted with Eqs. (2)–(5). The obtained parameters are summarized in Table III, and the calculated results are shown by the solid curves in Figs. 4–9. The measured spectra were fairly well reproduced.

The width parameter σ in Eq. (2) ranges from 70–140 MeV/c depending on the combination of the target and projectile. Since the value of σ corresponds to a single Cartesian component of the three momentum, one obtains $\sigma^2 = \langle \mathbf{p}^2 \rangle / 3$. This relates to the known Fermi motion, P_F , as $P_F^2 = 5 \langle \mathbf{p}^2 \rangle / 3$. Thus, we found that the obtained widths are consistent with the measured Fermi motion [23]. Velocity β of this component is almost the same as that of the projectile, and is independent of the target mass. These features are consistent with a picture that this component can be attributed to the projectile-fragmentation process.

The temperature of the preequilibrium component increases with increasing projectile energies and mass. This tendency is also reported in Refs. [13,24]. The velocity is roughly one-half of the beam velocity for the C target, and decreases to about one-third for the Pb target. This suggests that the mass of a source corresponding to the preequilibrium process increases with increasing target mass.

On the other hand, the temperature of the equilibrium component is less than 10 MeV. In addition, the velocity of this component is close to zero. Thus, this component is attributed to neutrons evaporated from an excited target residue.

Having integrated the function $d^2\sigma/dE_n d\Omega$ of the moving-source model with respect to the neutron energy above 10 MeV, we obtained angular distributions $d\sigma/d\Omega$ as

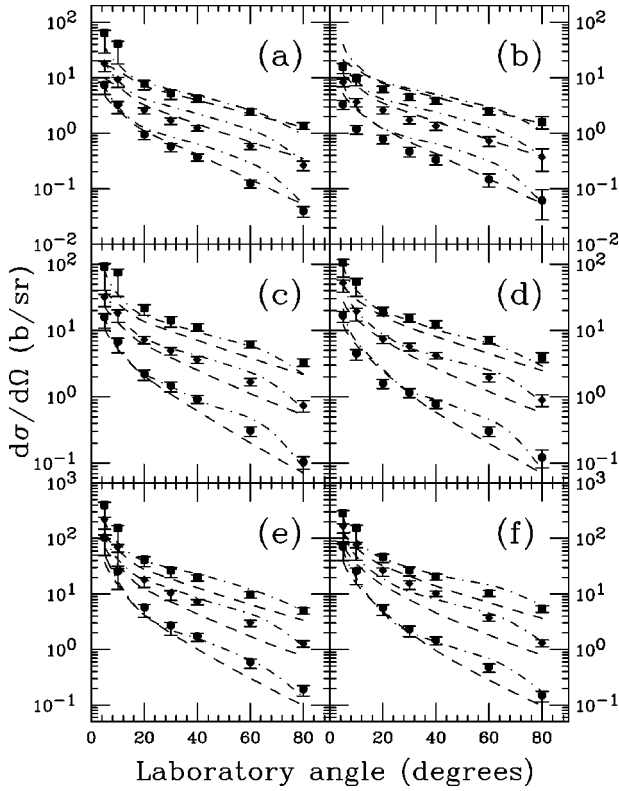


FIG. 10. Angular distributions $d\sigma/d\Omega$ as functions of the laboratory angle θ for (a) C at $E/A=290$ MeV, (b) C at $E/A=400$ MeV, (c) Ne at $E/A=400$ MeV, (d) Ne at $E/A=600$ MeV, (e) Ar at $E/A=400$ MeV, and (f) Ar at $E/A=560$ MeV. The circles, diamonds, and squares correspond to the $d\sigma/d\Omega$ for the C, Cu, and Pb targets, respectively. The results calculated by the QMD code and HIC are shown by the dashed and dot-dashed curves, respectively. The error bars include the statistic and systematic uncertainties.

shown in Fig. 10. The circles, diamonds, and squares in the figure represent $d\sigma/d\Omega$ for the C, Cu, and Pb targets, respectively. The error bars include the statistical and systematic uncertainties. A major source of the uncertainties at forward direction originates from the contribution of neutrons produced in the aluminum window, trigger detector and air; this contribution was estimated to be about 10–50 % at 5° , depending on the target and projectile, and was almost negli-

gible at backward angles as shown by the error bars in Fig. 10. The angular distributions show an exponential behavior as observed in similar measurements [10,11]. To determine the total cross sections σ_{tot} , the angular distributions were integrated with respect to the solid angle Ω . Due to limited coverage of the detection angle, the integration was made between 5° and 80° in polar angles θ . The integrated cross sections, $\sigma(5^\circ \leq \theta \leq 80^\circ)$, as functions of the target mass numbers are summarized in Table IV and plotted in Fig. 11. The integrated cross sections for the C beam at $E/A=400$ MeV are smaller than those at $E/A=290$ MeV. The difference can be explained by appreciable attenuation of neutrons in the target because of the relatively thick target used at $E/A=400$ MeV. For all projectiles, the integrated cross sections clearly depend on the projectile or target mass, but are less dependent on projectile energies. The integration of the cross sections was extrapolated to cover the entire solid angles using the fitted functions. The total cross sections σ_{tot} integrated with respect to the neutron energy above 10 MeV and the entire solid angles are listed in Table IV. The total cross sections σ_{tot} are larger by 10–20 % than the integrated cross sections, $\sigma(5^\circ \leq \theta \leq 80^\circ)$.

The neutron multiplicity for $E_n \geq 10$ MeV was estimated by dividing the total cross section σ_{tot} by the geometric cross section σ_g of the respective projectile-target system. The geometric cross section was calculated as $\sigma_g = \pi(R_p + R_T)^2$, where R_p and R_T are the radii of the projectile and the target nuclei, respectively. The radius was assumed to be $R = 1.2A^{1/3}$. The obtained values of the multiplicities are summarized in Table V. The multiplicities increase with the projectile or target mass. In particular, they are approximately proportional to the projectile mass.

B. Comparison with the QMD code and HIC

The measured neutron spectra $d^2\sigma/dE_n d\Omega$ were compared with those calculated by the QMD code [16] and HIC [17]. Similar comparisons were reported for Nb on Nb at $E/A=800$ MeV [10], Au on Au at $E/A=800$ MeV [10], and Ne on Pb at $E/A=790$ MeV [11]. It was reported that none of these codes could reproduce an overall agreement with the measured differential cross sections.

The QMD is a quantum extension of the classical molecular-dynamics model. In the model, each nucleon state

TABLE IV. Integrated cross sections $\sigma(5^\circ \leq \theta \leq 80^\circ)$ and total cross sections σ_{tot} for neutrons with $E_n \geq 10$ MeV. The errors include the statistic and systematic uncertainties.

Beam (MeV)	Cross sections σ (b)					
	C target		Cu target		Pb target	
	$\sigma(5^\circ \leq \theta \leq 80^\circ)$	σ_{tot}	$\sigma(5^\circ \leq \theta \leq 80^\circ)$	σ_{tot}	$\sigma(5^\circ \leq \theta \leq 80^\circ)$	σ_{tot}
C at $E/A=290$	$1.86^{+0.29}_{-0.42}$	$2.13^{+0.33}_{-0.48}$	$6.08^{+0.86}_{-1.13}$	$7.32^{+1.04}_{-1.37}$	$22.1^{+3.3}_{-6.7}$	$29.1^{+4.3}_{-8.8}$
C at $E/A=400$	$1.43^{+0.36}_{-0.37}$	$1.68^{+0.42}_{-0.43}$	$6.08^{+1.20}_{-1.25}$	$7.06^{+1.49}_{-1.55}$	$17.0^{+2.7}_{-3.0}$	$23.8^{+3.8}_{-4.2}$
Ne at $E/A=400$	$4.37^{+0.68}_{-0.98}$	$5.07^{+0.79}_{-1.14}$	$15.8^{+2.3}_{-2.8}$	$18.7^{+2.7}_{-3.4}$	$52.8^{+7.4}_{-14.2}$	$67.0^{+9.4}_{-18.0}$
Ne at $E/A=600$	$3.74^{+0.62}_{-0.70}$	$4.62^{+0.76}_{-0.86}$	$18.7^{+2.6}_{-3.2}$	$22.9^{+3.2}_{-4.0}$	$57.2^{+8.0}_{-10.9}$	$74.0^{+10.4}_{-14.1}$
Ar at $E/A=400$	$10.7^{+1.7}_{-4.1}$	$14.4^{+2.3}_{-5.6}$	$37.0^{+5.1}_{-11.9}$	$48.0^{+6.6}_{-15.4}$	$96.9^{+13.7}_{-31.6}$	130^{+18}_{-42}
Ar at $E/A=560$	$9.60^{+1.57}_{-3.19}$	$11.9^{+1.9}_{-3.9}$	$49.0^{+6.4}_{-12.4}$	$56.6^{+7.4}_{-14.3}$	102^{+14}_{-27}	131^{+18}_{-35}

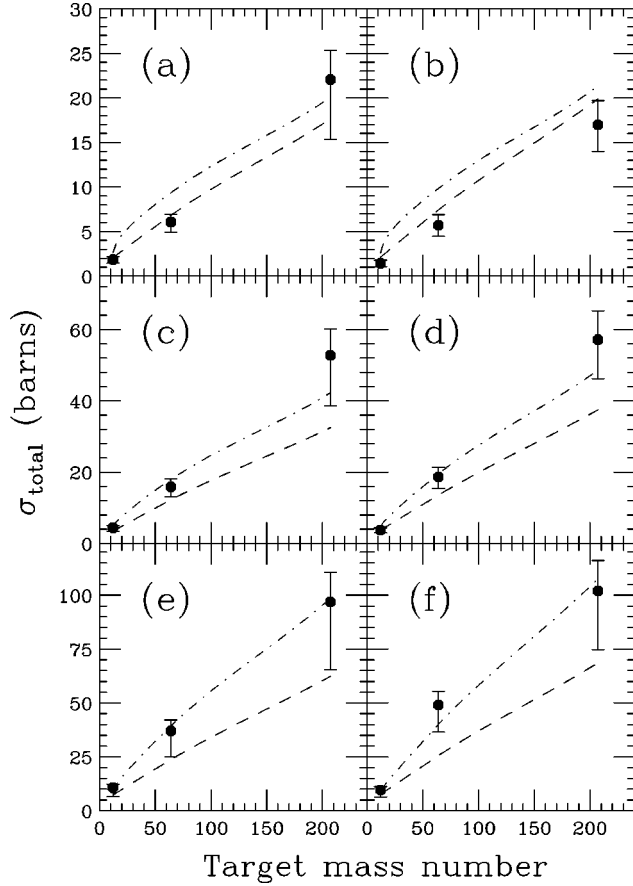


FIG. 11. Integrated cross sections $\sigma(5^\circ \leq \theta \leq 80^\circ)$, as functions of the target mass numbers for (a) C at $E/A=290$ MeV, (b) C at $E/A=400$ MeV, (c) Ne at $E/A=400$ MeV, (d) Ne at $E/A=600$ MeV, (e) Ar at $E/A=400$ MeV, and (f) Ar at $E/A=560$ MeV. The results calculated by the QMD code and HIC are shown by the dashed and dot-dashed curves, respectively. The error bars include the statistic and systematical uncertainties.

is described by a Gaussian wave function, and the time evolution of the A -body phase-space distribution is calculated. The QMD calculation code used here consisted of two parts: the QMD and the statistical decay model (SDM). The QMD simulation yields many nucleons and clusters. Then, the code switches to the SDM simulation that describes the statistical decay of the excited clusters. A detailed description of the

TABLE V. Neutron multiplicities $\sigma_{\text{tot}}/\sigma_g$ for the neutrons with $E_n \geq 10$ MeV.

Beam (MeV)	Multiplicities		
	C target	Cu target	Pb target
C at $E/A=290$	2.2	4.1	9.5
C at $E/A=400$	1.8	3.9	7.8
Ne at $E/A=400$	4.5	7.7	20
Ne at $E/A=600$	4.1	9.2	22
Ar at $E/A=400$	9.8	19	33
Ar at $E/A=560$	8.1	23	33

models is given elsewhere [25]. The HIC is a Monte Carlo code that calculates the transitions between continuum states in projectile and target nuclei. The model treats a heavy-ion collision as the interaction of two nuclei, expressed by the Fermi-gas model, passing through each other. During the overlap of two nuclei, cascade collisions take place, which result in the emission of free nucleons. The remaining parts are highly excited and emit evaporation particles. When they lose too much excitation energy to emit any remaining particles, the reaction is considered to be completed.

The neutron spectra calculated by the QMD code and HIC are shown by the dashed and dot-dashed curves, respectively, in Figs. 4–9. We found that the cross sections measured at the forward angles noticeably disagree with those calculated. The agreement becomes rather good as the laboratory angle increases. By integrating the calculated neutron spectra with respect to the neutron energy, one obtains the angular distributions. The angular distributions calculated by the QMD code and HIC are shown by the dashed and dot-dashed curves in Fig. 10. To make a quantitative comparison between the measured and calculated cross sections, we define the ratio R as $R = [(d\sigma/d\Omega)_m - (d\sigma/d\Omega)_c] / (d\sigma/d\Omega)_m$, where m and c refer to the measured and calculated $d\sigma/d\Omega$, respectively. The ratios R are plotted in Figs. 12 and 13 for the QMD code and HIC, respectively, as functions of laboratory angles. The QMD calculation underestimates the measured cross sections at the forward angles, namely, 5° and 10° , for all projectiles. For the C beam at $E/A=290$ MeV, the calculated $d\sigma/d\Omega$ from 20° – 80° agree with the measured one within 30%. An overestimation for the C beam at $E/A=400$ MeV has an origin in small measured cross sections due to the thick target used in this case. For the Ne and Ar beams, the QMD code underestimates the measured one by 30–50% for all angles. This tendency of underestimation was also reported in Ref. [11]. In contrast to the QMD code, the agreement of the HIC is rather good for the Ne and Ar beams. However, the disagreement is significant for the C beam.

The total cross sections calculated by the QMD code and HIC are displayed by the dashed and dot-dashed curves in Fig. 11, respectively. Although the QMD code reproduces the measured cross sections for the C beam, it underestimates those for the Ne and Ar beams. On the other hand, the agreement of the HIC with the measured cross sections is good for the heavy projectiles and targets, and is poor for light ones. This tendency is also reported in Ref. [7].

V. SUMMARY

We have carried out a systematic measurement of the double-differential cross sections for the neutron production. The neutron spectra measured at forward angles have a prominent peak originating from the projectile-fragmentation process. The spectra at backward angles have two components that are attributable to the preequilibrium and equilibrium processes. The neutron spectra were fairly well described by a moving-source model with those components. The parameters obtained by the fit were consistent with known pictures of projectile fragmentation, preequilibrium

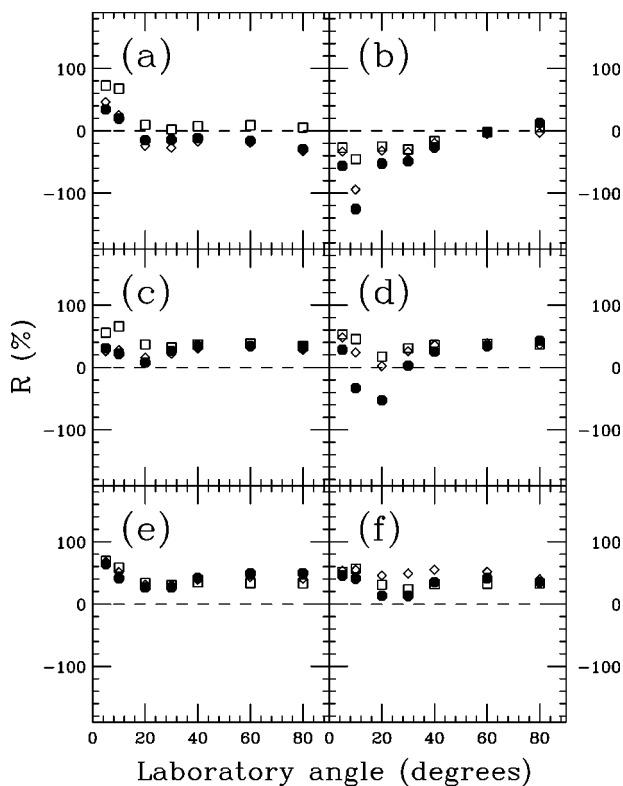


FIG. 12. Ratios R calculated by the QMD code for (a) C at $E/A=290$ MeV, (b) C at $E/A=400$ MeV, (c) Ne at $E/A=400$ MeV, (d) Ne at $E/A=600$ MeV, (e) Ar at $E/A=400$ MeV, and (f) Ar at $E/A=560$ MeV. The filled circles, open diamonds, and open squares show the ratios for the C, Cu, and Pb targets, respectively.

and equilibrium processes. By integrating the fitted functions with respect to the neutron energies and solid angles, the angular distributions and total cross sections were determined for $E_n \geq 10$ MeV.

The measured spectra, angular distributions and total cross sections were compared with those calculated by the QMD code and HIC. The QMD code roughly reproduced the measured cross sections for C beams. However, it underestimated them for the heavier projectiles by 30–50 %, such as Ne and Ar. On the other hand, the agreement of HIC with the measured cross sections was rather good for heavier projectiles and targets. Neither of the codes could reproduce the

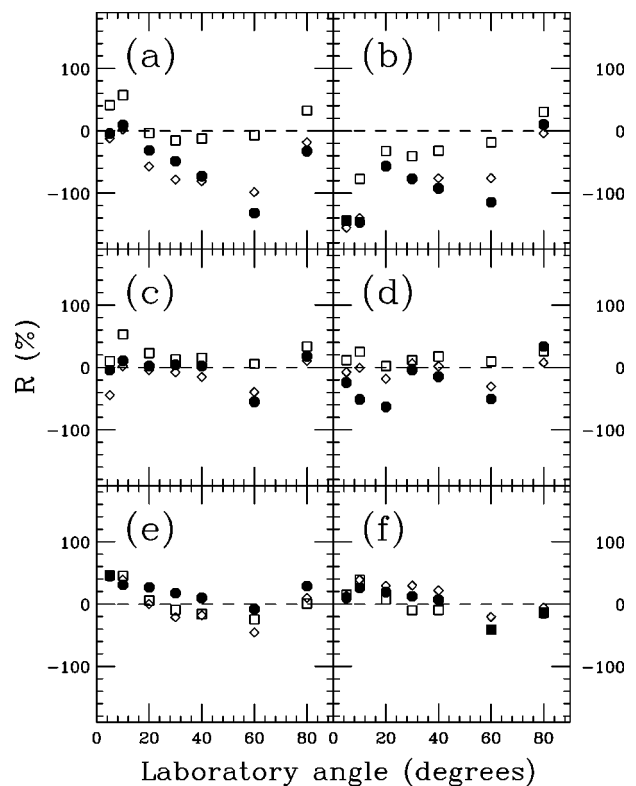


FIG. 13. Same as Fig. 12, but for the HIC. See the caption of Fig. 12.

measured cross sections for all combinations of the projectiles and targets.

ACKNOWLEDGMENTS

We would like to thank Michiya Sasaki, Hiroshi Yashima, and Taishi Shiomi during the experiment. We also thank the NIRS and the crew of Accelerator Engineering Corporation for support in the experiment and for efficient operation of the HIMAC. This work was carried out as a program of the research project with heavy ions at NIRS-HIMAC. It was also supported by the U.S. National Science Foundation under Grant No. 95-28844 (NSCL); NASA Contract No. H-29456D and Grant number L14230C through the U.S. DOE under Contract No. AC03076SF00098 (LBNL). L.H. and R.M.R. wish to thank the NIRS for its support and hospitality during their visits.

- [1] R.A. Cecil, B.D. Anderson, A.R. Baldwin, R. Madey, A. Galonsky, P. Miller, L. Young, and F.M. Waterman, *Phys. Rev. C* **21**, 2471 (1980).
 [2] L. Heilbronn, R. Madey, M. Elaasar, M. Htun, K. Frankel, W.G. Gong, B.D. Anderson, A.R. Baldwin, J. Jiang, D. Keane, M.A. McMahan, W.H. Rathbun, A. Scott, Y. Shao, J.W. Watson, G.D. Westfall, S. Yennello, and W.-M. Zhang, *Phys. Rev. C* **58**, 3451 (1998).
 [3] L. Heilbronn, R.S. Cary, M. Cronqvist, F. Deák, F. Frankel, A.

- Galonsky, K. Holabird, Á. Horváth, Á. Kiss, J. Kruse, R.M. Ronningen, H. Schelin, Z. Seres, C.E. Stronach, J. Wang, P. Zecher, and C. Zeitlin, *Nucl. Sci. Eng.* **132**, 1 (1999).
 [4] G. Li, T. Zhang, Z. Li, Y. Su, and S. Zhang, *Nucl. Instrum. Methods Phys. Res. A* **431**, 194 (1999).
 [5] T. Kurosawa, N. Nakao, T. Nakamura, Y. Uwamino, T. Shibata, N. Nakanishi, A. Fukumura, and K. Murakami, *Nucl. Sci. Eng.* **132**, 30 (1999).
 [6] T. Kurosawa, N. Nakao, T. Nakamura, Y. Uwamino, T. Shi-

- bata, A. Fukumura, and K. Murakami, *J. Nucl. Sci. Technol.* **36**, 41 (1999).
- [7] T. Kurosawa, N. Nakao, T. Nakamura, H. Iwase, H. Sato, Y. Uwamino, and A. Fukumura, *Phys. Rev. C* **62**, 044615 (2000).
- [8] R. Madey, W.-M. Zhang, B.D. Anderson, A.R. Baldwin, B.S. Flanders, W. Pairsuwan, J. Varga, J.W. Watson, and G.D. Westfall, *Phys. Rev. C* **38**, 184 (1988).
- [9] R.A. Cecil, B.D. Anderson, A.R. Baldwin, R. Madey, W. Schimmerling, J.W. Kast, and D. Ortendahl, *Phys. Rev. C* **24**, 2013 (1981).
- [10] R. Madey, W.-M. Zhang, B.D. Anderson, A.R. Baldwin, M. Elaasar, B.S. Flanders, D. Keane, W. Pairsuwan, J. Varga, J.W. Watson, G.D. Westfall, C. Hartnack, H. Stöcker, and K. Frankel, *Phys. Rev. C* **42**, 1068 (1990).
- [11] A.R. Baldwin, R. Madey, W.-M. Zhang, B.D. Anderson, D. Keane, J. Varga, J.W. Watson, G.D. Westfall, K. Frankel, and C. Gale, *Phys. Rev. C* **46**, 258 (1992).
- [12] G.D. Westfall, B.V. Jacak, N. Anantaraman, M.W. Curtin, G.M. Crawley, C.K. Gelbke, B. Hasselquist, W.G. Lynch, D.K. Scott, B.M. Tsang, M.J. Murphy, T.J.M. Symons, R. Legrain, and T.J. Majors, *Phys. Lett.* **116B**, 118 (1982).
- [13] B.V. Jacak, G.D. Westfall, C.K. Gelbke, L.H. Harwood, W.G. Lynch, D.K. Scott, H. Stöcker, M.B. Tsang, and T.J.M. Symons, *Phys. Rev. Lett.* **51**, 1846 (1983).
- [14] C. Bloch, W. Benenson, A.I. Galonsky, E. Kashy, J. Heltsley, L. Heilbronn, M. Lowe, R.J. Radtke, B. Remington, J. Kasagi, and D.J. Morrissey, *Phys. Rev. C* **37**, 2469 (1988).
- [15] A. Kiss, F. Deák, Z. Seres, G. Caskey, A. Galonsky, L. Heilbronn, and B. Remington, *Phys. Rev. C* **38**, 170 (1988).
- [16] J. Aichelin, *Phys. Rep.* **202**, 233 (1991).
- [17] H.W. Bertini, T.A. Gabriel, R.T. Santoro, O.W. Hermann, N.M. Larson, and J.M. Hunt, Oak Ridge National Laboratory Report No. ORNL-TM-4134, 1974 (unpublished).
- [18] Y. Hirao, H. Ogawa, S. Yamada, Y. Sato, T. Yamada, T. Murakami, A. Kitagawa, K. Sato, A. Itano, M. Kumada, E. Takada, M. Kanazawa, K. Noda, M. Sudou, K. Kawachi, F. Soga, M. Endo, T. Kanai, S. Minohara, H. Koyama-Ito, and T. Kohno, Annual Report HIMAC, National Institute of Radiological Sciences, NIRS-M-89/HIMAC-001, 1992 (unpublished).
- [19] K. Sato, S. Yamada, H. Ogawa, K. Kawachi, N. Araki, A. Itano, M. Kanazawa, A. Kitagawa, T. Kohno, M. Kumada, T. Murakami, M. Muramatsu, K. Noda, S. Sato, Y. Sato, E. Takada, A. Tanaka, K. Tashiro, M. Torikoshi, J. Yoshizawa, M. Endo, Y. Furusawa, T. Kanai, H. Koyama-Ito, N. Matsufuji, S. Monohara, N. Miyahara, F. Soga, M. Suzuki, H. Tomura, and Y. Hirao, *Nucl. Phys.* **A588**, 229c (1995).
- [20] R.A. Cecil, B.D. Anderson, and R. Madey, *Nucl. Instrum. Methods* **161**, 439 (1979).
- [21] N. Nakao, T. Nakamura, M. Baba, Y. Uwamino, N. Nakanishi, H. Nakashima, and S. Tanaka, *Nucl. Instrum. Methods Phys. Res. A* **362**, 454 (1995).
- [22] R. Serber, *Phys. Rev.* **72**, 1008 (1947)
- [23] E.J. Moniz, I. Sick, R.R. Whitney, J.R. Ficenece, R.D. Kephart, and W.P. Trower, *Phys. Rev. Lett.* **26**, 445 (1971).
- [24] J. Gosset, H.H. Gutbrod, W.G. Meyer, A.M. Poskanzer, A. Sandoval, R. Stock, and G.D. Westfall, *Phys. Rev. C* **16**, 629 (1977).
- [25] K. Niita, S. Chiba, T. Maruyama, T. Maruyama, H. Takada, T. Fukahori, Y. Nakahara, and A. Iwamoto, *Phys. Rev. C* **52**, 2620 (1995).